Zhao, Huawang; Chen, Xiaoyin; Bhat, Adarsh; Li, Yongdan; Schwank, Johannes W.

Insight into hydrothermal aging effect on deactivation of Pd/SSZ-13 as low-temperature NO adsorption catalyst: Effect of dealumination and Pd mobility

Published in:
Applied Catalysis B: Environmental

DOI:
10.1016/j.apcatb.2020.119874

Published: 05/06/2021

Document Version
Peer-reviewed accepted author manuscript, also known as Final accepted manuscript or Post-print

Please cite the original version:
Zhao, H., Chen, X., Bhat, A., Li, Y., & Schwank, J. W. (2021). Insight into hydrothermal aging effect on deactivation of Pd/SSZ-13 as low-temperature NO adsorption catalyst: Effect of dealumination and Pd mobility. *Applied Catalysis B: Environmental*, *286*, Article 119874. https://doi.org/10.1016/j.apcatb.2020.119874

Insight into hydrothermal aging effect on deactivation of Pd/SSZ-13 as low-temperature NO adsorption catalyst: Effect of dealumination and Pd mobility

Huawang Zhao [a,b,d], *Xiaoyin Chen* [a], *Adarsh Bhat* [a], *Yongdan, Li* [b,c], *Johannes W. Schwank* [a*]

[a] *Department of Chemical Engineering, University of Michigan, Ann Arbor, MI 48109, USA*

[b] *Collaborative Innovation Center of Chemical Science and Engineering (Tianjin), Tianjin Key Laboratory of Applied Catalysis Science and Technology, State Key Laboratory of Chemical Engineering (Tianjin University), School of Chemical Engineering, Tianjin University, Tianjin, 300072, China*

[c] *Department of Chemical and Metallurgical Engineering, School of Chemical Engineering, Aalto University, Espoo, 02150, Finland*

[d] *Department of Environmental Science & Engineering, College of Chemical Engineering, Huaqiao University, Xiamen, Fujian 361021, China*

Abstract: The Pd/SSZ-13 with the same Pd loading (1 wt.%) but different Si/Al ratio (6 and 13) were hydrothermal aged at 800, 850, and 900 ºC, respectively. The Pd/SSZ-13 with a lower Si/Al ratio suffers a more severe deactivation. The Pd/SSZ-13 with a Si/Al ratio of 6 experiences structural damage due to dealumination, while the structure of the sample with a Si/Al ratio of 13 remains intact. The agglomeration of Pd^{2+} ions to large PdO particles on the external surface of zeolite causes the deactivation. The Pd cations are mobile during aging. It indicates that, besides dealumination, the Pd^{2+} ions might be hydrolyzed and own a high mobility, which also results in

---

[*] Corresponding author: E-mail addresses: schwank@umich.edu (J.W. Schwank).

the Pd^{2+} ions agglomeration. The severe dealumination causes the deactivation after aging at 900 ºC. However, the Pd mobility might be the primary reason for the decline of NO adsorption capacity of Pd/SSZ-13 after aging at 800 and 850 °C.

Keywords: Low-temperature NO adsorption; Pd/SSZ-13; Hydrothermal aging; Dealumination; Pd mobility

1. Introduction

With the NO_x emission standard for vehicles tending to zero, advanced after-treatment techniques are necessary. The selective catalytic reduction by NH_3 (NH_3-SCR) technique is widely used to reduce NO_x emission [1]. The commercial NH_3-SCR catalysts, such as Cu-CHA catalysts, can achieve almost 100 % NO_x conversion when the exhaust temperature reaches above 200 °C [2, 3]. However, the SCR catalysts show an insufficient deNO_x activity during the cold start period where the exhaust temperature is below 200 °C. The promising strategy to control the NO_x emission during cold start is temporarily trap/store the NO_x at low temperatures and release them above 200 °C, where the SCR catalysts downstream are functional [4-7]. This technique is called passive NO_x adsorbers (PNA).

Ceria based materials were first investigated as PNA catalysts, while the facile sulfur poisoning limits the application [4]. Since 2016, Pd/BEA, Pd/ZSM-5, and Pd/SSZ-13 attract significant attention in low-temperature NO storage, because of the high NO storage capacity and high SO_2 poisoning resistance [4, 8]. The Pd^{2+} ions in Pd/zeolite are believed as the trapping sites for NO, while the adsorption mechanism is still debatable [4, 9, 10]. Chen *et al.* [4] and Khivantsev *et al.* [9, 11] proposed that Pd^{2+} ions stored the NO as $Pd^{2+}(NO)$. Following a different pathway, some authors proposed that Pd^{2+} ions adsorb NO as $Pd^{+}(NO)$ by reducing the

Pd^{2+} to Pd^{+} [10, 12]. The three catalysts exhibit different adsorption/release characteristics, because of different topological supports [8]. Compared to Pd/ZSM-5 and Pd/BEA, Pd/SSZ-13 exhibits appropriate NO_x release temperature ranges (200-400 ºC), while the starting release temperature of Pd/ZSM-5 and Pd/BEA is much lower (below 200 ºC), where the SCR catalysts down steam are still not warmed up [8, 13-15], indicating the advantage of Pd/SSZ-13 in application.

Since the PNA catalyst is exposed to high temperature with moisture due to the occasional regenerations of a diesel particulate filter, the high hydrothermal stability is necessary for a PNA catalyst. It has been found that Pd/SSZ-13 shows higher hydrothermal stability than Pd/BEA and Pd/ZSM-5 [14, 16]. Besides, Ryou *et al.* [17, 18] obtained that the NO adsorption capacity of Pd/SSZ-13 with dominant PdO was improved after a moderate hydrothermal treatment (750 ºC), attributed to the transformation of PdO to Pd^{2+} ions *via* hydrolysis. The similar positive effect on Pd/zeolite catalysts were also observed in other recent works [6, 19]. However, Khivantsev *et al.* [16] found that, Pd^{2+} cations were agglomerated to PdO in the Pd/SSZ-13 after hydrothermal aging at 750 ºC, where all the Pd stay as Pd^{2+} ions, resulting in a minor decline of NO storage capacity. Theis *et al.* [15] and Shan *et al.* [20] also observed the deactivation of Pd/CHA catalysts after aging at 800 ºC. Recently, Wang *et al.* [21] compared the hydrothermal stability of Pd/SSZ-13 and Pd/LTA catalysts with similar Si/Al ratio (15). They found that Pd/LTA exhibited a superior hydrothermal stability than Pd/SSZ-13 upon aging at 900 ºC. Despite the above significant studies, the deactivation process of Pd/SSZ-13 during aging is still poorly investigated, especially when the aging temperature is above 800 ºC. In comparison, the hydrothermal aging effect on Cu-SSZ-13 catalysts has been well-studied [2, 22-24]. The harsh aging condition lead to dealumination and agglomeration of the SCR active Cu^{2+} sites to CuO_x, which are considered the two main factors resulting in the deactivation of Cu-SSZ-13 [2, 24, 25]. The atomic-level of the relationship between the two factors was also investigated [26, 27]. However, such investigations on Pd/SSZ-13 are still lacking.

This study aims at investigating the deactivation process of Pd/SSZ-13 catalysts during aging. The hydrothermal stability of Pd/SSZ-13 catalysts with the same Pd loading (1 wt.%) but different Si/Al ratio (6 *vs.* 13) was compared. The structure changes and variation of Pd state after aging at different temperatures (800, 850, and 900 ºC) were characterized. The deactivation mechanism is discussed by comparing different changes of the two serious Pd/SSZ-13 catalysts after aging. The contributions of dealumination and Pd mobility on the deactivation of Pd/SSZ-13 are analyzed.

2. Experimental

2.1. Catalyst Preparation

Na-SSZ-13 (Si/Al=6, determined by ICP-MS) was synthesized following the previous procedures [28]. The NH_4-SSZ-13 with a Si/Al ratio of 13 was purchased from ACS material.

The Pd/SSZ-13 catalysts were prepared by incipient wetness impregnation. Firstly, the calcined Na-SSZ-13 (Si/Al of 6) was transformed into NH_4-SSZ-13 *via* ion-exchange with a 5 M $(NH_4)_2SO_4$ solution at 80 °C for 2.5 h. NH_4-SSZ-13 was then impregnated by an appropriate amount of palladium nitrate solution (Alfa Aesar) to prepare Pd/SSZ-13 with 1 wt.% Pd loading. The wetted catalyst precursor was dried at ambient conditions for 6 h and then dried at 60 °C for 8 h. After calcination at 600 °C, the catalysts were obtained. The preparation of Pd/SSZ-13 with a Si/Al ratio of 13 followed the same Pd loading and calcination procedures above. The two types of Pd/SSZ-13 catalysts were denoted as 1 Pd (6) and 1 Pd (13), respectively. H-SSZ-13 sample was prepared by calcining NH_4-SSZ-13 (Si/Al=6 and 13) at 600 ºC in the air for 5 h, denoted as H-SSZ (6) and H-SSZ (13), respectively.

The hydrothermal aging (HTA) treatment was performed in synthetic air containing 10% H_2O at 800, 850 or 900 °C for 16 h, respectively. The aged samples are abbreviated as 1 Pd (X)-800, 1 Pd (X)-850, and 1 Pd (X)-900, respectively, according to their different HTA temperature, where X represents the Si/Al ratio of the SSZ-13.

2.2. NO Storage and Release

The storage and release experiments of NO were carried out in a fixed-bed quartz tube reactor (4 mm inner diameter) under a simulated realistic (5% H_2O-5% CO_2) exhaust conditions. Mass flow controllers controlled the flow rates. The catalyst temperature was monitored and controlled by two K-type thermocouples located upstream and downstream of the catalyst bed. Deionized water was fed by a D-Series syringe pump (Teledyne Isco). The main gas tubing was heated to 120 °C by heating tapes to fully vaporize liquid water in the entire lines down to the FTIR gas analyzer. 50 mg of powder catalyst (250-420 μm) was used and was diluted with the same size silica gel (50 mg, Sigma Aldrich Davisil Grade, calcined at 800 °C for 4 h). During the storage and release processes, the feeding gases were adjusted to contain 200 ppm NO, 10% O_2, 5% H_2O, 5% CO_2, and balanced with N_2. The gas concentrations (such as NO, N_2O, and NO_2) during the reactions were measured online by a gas FTIR analyzer (Antaris™ IGS).

The pretreatment on Pd/SSZ-13 catalyst was carried out before the storage and release. In each test, the catalyst was first pretreated at 600 °C with a flow of 10 % O_2/N_2 for 30 min and another 30 min with a flow of 10 % O_2-5 % H_2O-N_2 at a rate of 250 mL/min. The catalyst was then cooled to 100 °C for NO storage under the same feed rate, corresponding to a weight hourly space velocity (MHSV) of 300,000 $mL \cdot h^{-1} \cdot g^{-1}$. The gas concentrations were first stabilized in a bypass line of the reactor, and then switched to the catalysts for NO adsorption (10 min) at 100 °C. This adsorption stage was then followed by a release stage where the temperature increased to 600 ºC at a ramping rate of 10 ºC/min under the same gas mixture feed. The total NO adsorption value was calculated by integrating the NO release profiles in 200-480 °C to illustrate the NO adsorption capacity of each sample at low temperatures (below 200 °C).

2.3. Catalyst Characterization

N_2 physisorption was carried out at -196 °C on a Micromeritics ASAP 2020 instrument to determine the specific surface area and pore volume of the catalysts. Before the analysis, the sample was pre-degassed in a vacuum at 350 °C for 24 h. The specific surface area was calculated using the BET equation. The micropore surface area and volume were estimated using the t-plot method. Powder X-ray diffraction (XRD) measurements were carried out on a Rigaku Ultima IV instrument using Cu Kα radiation ($\lambda = 1.54178$ Å) at 40 kV and 44 mA under ambient conditions. The scan angle was set from 5° to 55° using a step size of 0.01°, and data were accumulated at a rate of 0.083°/s. Transmission electron microscope (TEM) images were collected by a JEOL 2010F analytical electron microscope with accelerating voltage of 200 kV. Before taking the images, the powder catalyst was suspended in ethanol, dispersed by ultra-sonication, and then dropped onto lacey formvar/carbon 200 mesh copper grids (Ted Pella, Inc).

^{27}Al solid-state magic-angle spinning (MAS) nuclear magnetic resonance (NMR) were conducted on Varian Infinity plus 300 WB spectrometer utilizing a 4 mm triple resonance probe operating with the resonance frequencies of 78.13 MHz. $Al(NO_3)_3$ aqueous solution (1 mol/L) was used for ^{27}Al MAS NMR spectroscopy as references. The amount and volume of the samples in the NMR test were kept constant; thus, the resonances intensities can be compared. For the ^{27}Al MAS NMR spectra, the resonance peaks are deconvoluted using

Lorentzian/Gaussian, with the peak position not fixed for the best fit. All samples allow the fitting parameters in the deconvolution to be optimized.

In situ diffuse reflectance Fourier transform infrared spectroscopy (DRIFTs) experiments were carried out on a Bruker TENSOR 27 spectrometer with an MCT detector. The Pd/SSZ-13 catalyst was first ground by mortar grinding, and then loaded into a reactor chamber (Praying Mantis™) containing two ZnSe windows and a quartz window. Before collecting background spectra at the desired temperatures, the sample was pretreated at 550 °C for 1 h in flowing 20% O_2/N_2.

3. Results

3. 1. Performance of NO_x Adsorption and Release on Pd/SSZ-13

3.1.1 The NO Adsorption at 100 °C

Fig. 1a and 1b show the profiles of NO_x (including NO and NO_2) concentration against time on stream in the continuous reaction gas feed for the 1 Pd (6) and 1 Pd (13) before and after HTA, respectively. It is composed of by-pass feed (10 min), followed by NO storage (at 100 °C for 10 min), and subsequent release under the same gas feed conditions during the temperature ramping (10 °C/min up to 600 °C). The details of NO and NO_2 concentration during adsorption and release for fresh and HTA 1 Pd (6) and 1 Pd (13) samples are shown in Fig. 1c and 1d, respectively. Since the inlet concentration of NO was 200 ppm, negative peaks below 200 ppm baseline indicate the storage/adsorption of NO, and positive peaks above 200 ppm reflect the release/desorption. After switching the feed gases from by-pass to the catalyst, negative NO adsorption peaks at 100 °C were observed (Fig. 1c and d). Also, the NO_2 formation was not observed (Fig. 1c and 1d), suggesting the NO_x profiles coincide with the NO curves for all catalysts during NO adsorption at 100 °C for all samples.

After HTA, the 1 Pd (6)-800 showed a lower NO adsorption capacity than 1 Pd (6) at 100 ºC, while almost no adsorption peaks were observed in 1 Pd (6)-850 and 1 Pd (6)-900 samples (Fig. 1c). The 1 Pd (13) also exhibited a gradual NO adsorption capacity decline with the increase of HTA temperature (Fig. 1d). However, strong negative NO adsorption peaks were still found on 1 Pd (13)-800 and 1 Pd (13)-850 samples. Similar to the 1 Pd (6)-900, 1 Pd (13)-900 exhibited inert NO adsorption at 100 ºC.

3.1.2 Release After NO Storage

After NO adsorption at 100 °C, the release of stored NO_x in the same reactive gas feed occurs when the temperature increases from 100 to 600 °C for the 1 Pd (6) and 1 Pd (13), as shown in Fig. 1a and 1b, respectively. However, another NO_x adsorption peaks were observed in the 1 Pd (6) and 1 Pd (13) samples in the temperature range of 100-200 °C, attributed to the net impact of a big NO adsorption peak and a small NO_2 desorption peak at around 160 °C (Fig. 1c and 1d). In addition, the NO_x and NO adsorption peaks at around 160 °C are significantly decreased and almost disappear in all the HTA samples, independent of the Si/Al ratio and HTA temperatures. Also, the NO_2 formation peaks are almost vanished after HTA treatment.

The NO_x release peaks were observed at 210-480 °C without the desorption of NO_2, indicating that the NO_x release profiles coincide with the NO desorption curves for all the samples (Fig. 1a-d). Compared to 1 Pd (6), the NO release peak decreases after HTA at 800 °C, and almost disappear after HTA at 850 and 900 °C (Fig. 1c). The NO desorption peak shifts to higher temperature ranges for the 1 Pd (6)-800 sample (210-480 °C) compared to 1 Pd (6) sample (210-435 °C). The 1 Pd (13) shows a high NO release peak in 210-400 °C, while the peaks decrease and change to higher temperatures in 1 Pd (13)-800 (210-450 °C) and 1 Pd (13)-850 (210-450 °C) samples (Fig. 1d). The NO desorption profile is almost flat in 1 Pd (13)-900, consistent with the inert NO adsorption at 100 °C.

The quantitative NO storage content of each sample is obtained by integrating the NO release peaks in 200-480 °C, and the results are shown in Table 1. Compared to 1 Pd (6) (NO/Pd=0.70), 40%, 78%, and 93% of the NO storage capacity decline is observed in 1 Pd (6)-800 (0.42), 1 Pd (6)-850 (0.18), and 1 Pd (6)-900 (0.05), respectively. Compared to 1 Pd (13) (0.59), 19%, 32%, and 71% of the NO storage capacity decreases for the Pd (13)-800 (0.48), Pd (13)-850 (0.39), Pd (13)-900 (0.17) samples, respectively. It is worth pointing that 1 Pd (13) exhibits a lower NO storage content than 1 Pd (6), while the HTA 1 Pd (13) samples display higher NO storage capacity compared to the 1 Pd (6) samples aged at the same temperature, indicating that the 1 Pd (13) shows higher stability than 1 Pd (6).

NO_2 formation was observed above 480 °C for all fresh and HTA samples, as shown in Fig. 1c and 1d. Meanwhile, the NO concentration decreases, while the NO_x concentration remains constant at 200 ppm for all the samples (Fig. 1a and 1b), indicating that the NO_2 formation should be ascribed to the catalytic oxidation of NO to NO_2 (Fig. S1), in agreement with previous works [4, 8].

3.2. Pores and Crystallographic Structure

3.2.1 N_2-Physisorption Results

To investigate the effect of HTA on the pore structure of the Pd/SSZ-13 catalysts, the N_2-physisorption measurement was conducted, and the results are shown in Table 2. The 1 Pd (6) showed a high BET surface area of 457 m^2/g and a pore volume of 0.25 cm^3/g. Different extent of micropore volume decline was observed in the 1 Pd (6)-800 (43%), 1 Pd (6)-850 (48%), and 1 Pd (6)-900 (74%) samples after HTA, compared to 1 Pd (6). Besides, the 1 Pd (6)-800 and 1 Pd (6)-850 samples showed a higher volume of mesopore (V_{meso}) than 1 Pd (6), suggesting that a part of micropores is collapsed and expanded to mesopore after HTA at 800 and 850 °C. Only 0.07 cm^3/g of total pore volume remains in 1 Pd (6)-900, demonstrating that the 1 Pd (6) with a low Si/Al ratio suffers a severe degradation of the pore system upon aging at 900 °C.

The 1 Pd (13) showed a high BET surface area of 462 m^2/g and a pore volume of 0.28 cm^3/g. Micropores contribute 96% of the surface area and 79% of the total pore volume. The micropore volume of the HTA samples first increases with the temperature increasing from 800 to 850 °C, and then decreases when the aging temperature reached 900 °C. However, the micropore volume of 1 Pd (13)-900 is still higher than 1 Pd (13). It indicates that the pore systems are well-maintained in the aged samples, and blocks in the micropores are removed during HTA. Also, the V_{meos} increases with the increment of HTA temperature, revealing that a mild collapse of micropore expanding to mesopores occurs in 1 Pd (13).

3.2.2 XRD results

To further analyze the changes of structure and crystallinity of the samples after HTA, XRD characterizations were conducted, as shown in Figs. 2 and 3. Both H-SSZ (6) and 1 Pd (6) showed typical CHA structure, and no other diffraction peaks belonging to PdO ($2\theta=33.9$ and 46.6°) or Pd ($2\theta=40.1°$) were detected [29, 30], demonstrating that the non-exchanged Pd species, if exist, should be highly dispersed in 1 Pd (6) (Fig. 2a). The intensities of the CHA diffraction peaks decrease with the HTA temperature increasing from 800 to 900 °C. Besides, the PdO diffraction peaks at $2\theta=33.9$ and 46.6° were detected in HTA 1 Pd (6) samples (Fig. 2b), and the intensities of the peaks increase with the increment of HTA temperature, suggesting the more severe PdO sintering after aging at higher temperature.

Fig. 3 shows the XRD patterns of the H-SSZ (13), 1 Pd (13), and HTA 1 Pd (13) samples. Both H-SSZ (13) and 1 Pd (13) exhibited identical CHA diffraction peaks, and the diffraction peaks of PdO or Pd particles were also not observed (Fig. 3a), indicating the Pd is well-dispersed in 1 Pd (13). The CHA diffraction peaks show a slight decrease after HTA, indicating that the aged samples with high Si/Al ratio (13) remain a high crystallinity. No apparent PdO diffraction peaks (2θ=33.9 and 46.6 °) were observed in 1 Pd (13)-800 and 1 Pd (13)-850 samples, while such peaks were clearly observed in Pd/SSZ (13)-900 samples.

3.2.3 ^{27}Al MAS NMR results

XRD results (Fig. 2 and 3) present that Pd/SSZ-13 samples, especially for 1 Pd (6), suffer structure degradation after aging. The dealumination is considered the primary reason for structural damage of zeolite during HTA [31, 32]. The ^{27}Al MAS NMR technique would provide comprehensive information on the Al coordination environment in zeolites [33]. Therefore, the ^{27}Al MAS NMR measurements were conducted to understand the structure changes of the catalysts at the molecular level.

Fig. 4a presents ^{27}Al MAS NMR spectra of 1 Pd (6) samples before and after HTA. In these spectra, a main resonance peak at ~57.5 and a small peak at 0 ppm were observed, arising from tetrahedrally coordinated framework Al (TFAl) and octahedrally coordinated extra-framework Al (EFAl), respectively [28, 31]. Also, a new peak at 25 ppm was observed in HTA 1 Pd (6) samples, attributed to the penta-coordinated framework Al [34]. Taking the area of TFAl signal of 1 Pd (6) sample as reference, the amounts of TFAl in HTA samples are normalized, and the results are displayed above each spectrum. It shows that 73% and 60% of TFAl remain in the 1 Pd (6)-800 and 1 Pd (6)-850 samples, respectively, while significantly decreases to 25% after HTA at 900 °C.

Fig. 4b shows the ^{27}Al MAS NMR spectra of fresh and HTA 1 Pd (13) samples. Two resonance peaks at around 57.5 and 0 ppm were observed, attributed to TFAl and EFAl, respectively. The normalized TFAl amount of the samples is shown above each spectrum, using the peak area of TFAl in 1 Pd (13) as the unity. The amount of TFAl decreases to 71% and 62% in 1 Pd (13)-800 and 1 Pd (13)-850, respectively, and significantly decreases to 31% after HTA at 900 °C.

3.2.4 NH_3-DRIFTs Results

In Pd/SSZ-13 catalysts, only some parts of TFAl sites (Si-O-Al) are occupied by Pd^{2+} ions, and the rest framework Al sites are normally balanced by H (*i.e.*, Si-O(H)-Al), which provide Brønsted acid sites [9]. NH_3 adsorption DRIFTs measurements characterize OH vibrational (νOH) region of the catalysts, giving the information about the changes of the Brønsted acids sites in Pd/SSZ-13 after HTA.

As shown in Fig. 5a, four νOH features at 3740, 3654, 3625, and 3585 cm^{-1} were observed in 1 Pd (6) catalyst. The bands at 3740 and 3654 cm^{-1} can be assigned to terminal Si-OH and Al-OH, respectively, and the bands at 3625/3585 cm^{-1} are attributed to Brønsted acid sites (*i.e.*, Si-O(H)-Al) [26, 35]. After HTA at 800 ºC, the intensities of peaks for Si-O(H)-Al decreased, indicating that some parts of framework Al from Si-O(H)-Al are detached from zeolitic structure. Also, the intensity of terminal Si-OH (3740 cm^{-1}) diminishes with the HTA temperature increasing from 800 to 900 ºC, indicating the Si in the framework is detached.

As shown in Fig. 5b, four νOH features at 3738, 3670, 3625/3585 cm^{-1} were also observed in 1 Pd (13) catalyst. The intensities of 3625/3585 cm^{-1} peaks in 1 Pd (13) are much lower than 1 Pd (6), indicating the less content of Brønsted acid sites in the former one. Similar to Fig. 5a, the band intensities of Si-O(H)-Al are diminished in 1 Pd (13) after HTA at 800 ºC, indicating the occurrence of severe dealumination from Si-O(H)-Al in 1 Pd (13). However, it is worth knowing that the band of Si-OH almost remains constant with the HTA temperature increasing from 800 to 900 ºC, which even shows a little increase, indicating that most of the Si are still anchored in the framework after the detachment of some Al sites.

3.3 Characterizations of Pd species

3.3.1. NO-DRIFTs Results

NO can be adsorbed on Pd cations in Pd/SSZ-13 in the absence of H_2O, providing distinguishable FTIR spectra [9, 11]. Therefore, NO-DRIFTs were conducted to characterize the changes of Pd cations in Pd/SSZ-13 catalysts after HTA at different temperatures.

The FTIR spectra collected upon NO adsorption on fresh and HTA 1 Pd (6) are presented in Fig. 6a. Two main FTIR features at 1877 and 1824 cm^{-1} were observed in 1 Pd (6), assigned to the ν(NO) vibrations in Pd^{2+}-NO and Pd^{+}-NO, respectively [17, 21]. It is believed that two kinds of Pd cations, *i.e.,* Pd^{2+}-2Z (Z represents the Si-O-Al) and $Pd(OH)^{+}$, exist in Pd/SSZ-13, which are balanced by two close Al sites and a single Al site, respectively [10, 12, 21, 36]. Previous studies proposed that the formation of Pd^{+}-NO and Pd^{2+}-NO is attributed to the NO adsorption on $Pd(OH)^{+}$ and Pd^{2+}-2Z, respectively [10, 21]. Therefore, the relative intensity of peaks 1823/1877 cm^{-1} represents the changes of relative content of $Pd(OH)^{+}$ and Pd^{2+}-2Z in each sample.

The peak ratio of 1823/1877 cm^{-1} increases after HTA at 800 °C, as compared to 1 Pd (6), shown in Fig. 6a. It indicates the more severe loss of Pd^{2+}-2Z than Pd(OH)$^{+}$ in 1 Pd (6) after HTA at 800 °C. The NO adsorption IR peaks almost disappear in 1 Pd (6)-850 and 1 Pd (6)-900 samples, indicating that most of Pd cations are vanished in both samples.

Fig. 6b shows the NO adsorption spectra of fresh and HTA Pd (13) samples. The NO adsorption peaks at 1883 and 1827 cm^{-1} are distinguishable in fresh, 1 Pd (13)-800, and 1 Pd (13)-850 samples. The relative intensity of 1827/1883cm^{-1} increases with the increment of HTA temperature from 800 to 850 °C. Only very weak peaks are found in 1 Pd (13)-900 sample, indicating the significant decrease of Pd cations after HTA at 900 °C.

The comparison of Fig. 6a and Fig. 6b reveals that the Pd cations in 1 Pd (13) possess a higher resistance in agglomeration than in 1 Pd (6) after HTA at 800 and 850 °C, demonstrating the higher hydrothermal stability of 1 Pd (13) sample.

3.3.2. CO-DRIFTs Results

CO-DRIFTs are conducted to further analyze the changes of the Pd cations after HTA. The results are shown in Fig. 7. Fig. 7a shows CO adsorption FTIR results collected on fresh and HTA 1 Pd (6) samples. After the CO adsorption, several peaks centered at 2208/2187, 2142, and 2125 cm^{-1} were observed. The peaks at 2208/2187 cm^{-1} can be assigned to Pd^{2+}(CO)$_2$, where the Pd cations are stabilized by paired Al sites (Pd^{2+}-2Z) [11, 36]. The peak at 2142 cm^{-1} is ascribed to the Pd^{2+}(CO)(OH), where the Pd cations are stabilized by one Al sites and hydroxyl (Pd(OH)$^{+}$) [36, 37]. The peak at 2125 cm^{-1} is assigned to Pd^{2+}(OH)(CO) complex or alternatively Pd^{2+}(CO) complex [36]. Another peak at 1897 cm^{-1} in 1 Pd (6) can be ascribed to the CO adsorbed on small metallic Pd clusters as $Pd_x(CO)_y$, due to the reduction of small PdO to Pd by CO in N_2 [8, 11], indicating that PdO particles are formed in 1 Pd (6).

Two new peaks centered at 2161 and 2110 cm^{-1} were observed in 1 Pd (6)-800 and 1 Pd (6)-850 samples, as compared to 1 Pd (6). The peak at 2110 cm^{-1} is assigned to linearly-bound CO on Pd^0, attributed to the reduction of newly formed PdO in 1 Pd (6) after HTA [38]. However, the assignment of 2161 cm^{-1} is a little bit difficult, which will be discussed next.

Fig. 7b shows the FTIR results collected on fresh and HTA 1 Pd (13) samples. After CO adsorption, the peaks centered at 2208/2188 ($Pd^{2+}(CO)_2$), 2145 ($Pd^{2+}(OH)(CO)$), 2124 ($Pd^{2+}(OH)(CO)$ or $Pd^{2+}(CO)$), and 2162 cm^{-1} were observed [36]. The comparison of CO FTIR spectra of 1 Pd (6) and 1 Pd (13) suggests that the peak at 2162 cm^{-1} is only present in the 1 Pd (13), which has a high Si/Al ratio. It is known that the Pd^{2+}-2Z is preferentially formed in Pd/SSZ-13 with a low Si/Al ratio, which contains larger adjacent Al sites [16, 39]. Indeed, the relative intensity of CO adsorption peaks of Pd^{2+}-2Z (2208/2188 cm^{-1}) compared to $Pd(OH)^+$ (2142/2124 cm^{-1}) is higher in 1 Pd (6) than 1 Pd (13), which identifies that the Pd^{2+}-2Z account for a higher proportion of the total Pd cations in the former sample. Therefore, it is expected that 1 Pd (13) possesses larger content of $Pd(OH)^+$ than 1 Pd (6), since both samples have similar Pd loading (1 wt.%). In this sense, the 2162 cm^{-1}, not observed in 1 Pd (6), should be attributed to the CO adsorption on $Pd(OH)^+$, *i.e.*, $Pd(CO)(OH)^+$. It should be pointed that both peaks at 2145 and 2162 cm^{-1} are assigned to the CO adsorption on $Pd(OH)^+$, while the split of IR band of 17 cm^{-1} indicates that the two Pd cations might reside different locations in SSZ-13 [9].

Compared to other IR peaks for Pd^{2+} ions (2208/2188 cm^{-1} for Pd^{2+}-2Z and 2145 cm^{-1} for $Pd(OH)^+$), the relative intensity of 2162 cm^{-1} in 1 Pd (13) shows a gradual increase with the HTA temperature increasing from 800 to 850 °C. Besides, the peak at 2162 cm^{-1} is exclusively found in the HTA 1 Pd (6) samples, which was not observed in the fresh sample in Fig. 7a. It indicates that some $Pd(OH)^+$ (2161 cm^{-1}) ions are generated during HTA. This can be attributed to the migration of Pd^{2+}-2Z to $Pd(OH)^+$ or the $Pd(OH)^+$ migrating from one location (2145 cm^{-1}) to another (2161 cm^{-1}), suggesting that the Pd cations are movable in both 1 Pd (6) and 1 Pd (13) samples during HTA.

3.3.3 TEM Images

The NO- and CO-DRIFTs results (Fig. 6 and 7) show that the content of ionic Pd is reduced, and the XRD results (Fig. 2 and 3) further reveal that PdO particles are formed in both 1 Pd (6) and 1 Pd (13) samples after HTA. It indicates that some parts of Pd cations are agglomerated to PdO particles during HTA. The TEM images describe the size and location of the PdO particles.

Fig. 8 shows the TEM images of HTA 1 Pd (6) catalysts. Rather uniformly and highly dispersed PdO particles with the size of around 1.1 nm were observed in the fresh 1 Pd (6) in Fig. S2. However, large PdO particles are formed after HTA at 800 °C, with a diameter of around 8.5 nm, as shown in Fig. 8a. After HTA at 850 °C, large PdO particles with a diameter of 23.8 nm and several smaller PdO particles with a size of around 3 nm were found in the 1 Pd (6)-850 (Fig. 8b). With the increase of the aging temperature to 900 °C, only a large PdO particle with 43.2 nm diameter was observed on the external surface of 1 Pd (13)-900. Besides, no PdO particles exist in the inner of the zeolite (Fig. 8c). It indicates that Pd species in 1 Pd (6) tend to be agglomerated to large PdO particles on the external surface of the zeolite with the increase of HTA temperature.

Fig. 9 shows the TEM images of fresh and HTA 1 Pd (13) catalysts. The PdO particles are uniformly dispersed in the fresh sample, with the particle size of around 1.2 nm (Fig. 9a). The size and distribution of PdO particles in 1 Pd (13)-800 is almost identical to that in 1 Pd (13), shown in Fig. 9b. However, large PdO particles with a diameter of 2.6-6.5 and ~30 nm was observed in 1 Pd (13)-850 and 1 Pd (13)-900 samples, respectively (Fig. 9c and 9d). Also, large PdO particles (above 6 nm) are almost exclusively found on the external surface of the 1 Pd (13)-850 and 1 Pd (13)-900 samples, confirming the movement of Pd species from inner to the outside of the zeolite during HTA treatment, which agglomerates to large PdO particles, in agreement with previous works [16, 21].

4. Discussion

4.1 Effect of HTA on Structure and NO Adsorption/Release Performance

4.1.1 On Structure

The decrease in CHA diffraction peaks, shown in XRD results (Fig. 2), indicates that the crystallinity of 1 Pd (6) decreases with the increase of HTA temperature. ^{27}Al MAS NMR results (Fig. 4a) further show that some parts of framework Al sites are detached after HTA. The severe dealumination should contribute to the structural degradation (Fig. 2) and the loss of micropore volume (Table 2) in HTA 1 Pd (6) samples [16].

A slight decline in the intensities of diffraction peaks was observed in the 1 Pd (13) samples after HTA (Fig. 3), indicating that the long-range ordered crystal is well-maintained in the aged samples with a high Si/Al ratio. However, 1 Pd (13) and 1 Pd (6) present a similar dealumination after HTA at the same temperature (Fig. 4), suggesting that the dealumination has a less influence on the structure degradation of 1 Pd (13) than 1 Pd (6). This can be explained by the different framework Al content in both samples. 1 Pd (6) possesses much higher amount of Al in the framework than the 1 Pd (13). Thus, less content of TFAl is detached in 1 Pd (13) than 1 Pd

(6) after HTA despite showing similar dealumination (Fig. 4). On the other hand, the serious dealumination results in the detachment of framework Si (Fig. 5a), since the framework of zeolite is a network constructed by Si and Al, aggravating the structure degradation of 1 Pd (6) after HTA. In comparison, the detachment of framework Si was not observed in HTA 1 Pd (13) due to the less content of TFAl loss (Fig. 5b).

The well-maintained crystal contributes to the highly preserved micropore volume in HTA 1 Pd (13) samples (Table 2). The aged 1 Pd (13) samples show a higher micropore volume than the fresh sample (Table 2). The TEM results (Fig. 9) show that large PdO particles are formed on the external surface of the SSZ-13 crystal after HTA. It can be inferred that the movement of Pd species, located in the pore channels, from inner to the external surface of the zeolite free up the micropores, increasing the micropore volume of the aged samples.

4.1.2 On Performance

The NO storage capacity of 1 Pd (6) and 1 Pd (13) decreases with the increase of HTA temperature (Table 1). The decline of NO storage capacity should be attributed to the agglomeration of Pd^{2+} to PdO in the aged samples, as shown by XRD (Fig. 2 and 3) and TEM results (Fig. 8 and 9), since the Pd cations are believed as the NO adsorption sites while PdO particles are inactive [5, 6, 9, 14, 40].

An interesting observation in Fig. 1 is that the declining extent of the second NO_x adsorption peak at 160 °C is much greater than the peak at 100 °C. For example, the second NO_x adsorption peaks are almost vanished in both 1 Pd (6) and 1 Pd (13) after HTA at 750 °C, while only a minor decline is observed for the NO_x adsorption peaks at 100 °C. Also, the NO_2 formation peaks significantly decrease after HTA at 750 °C. These observations indicate that the HTA has different influence on the NO_x adsorption at 100 °C and 160 °C. According to the literature [10, 39, 41], the Pd^{2+} ions are solvated by H_2O during the NO adsorption in the presence of H_2O at low temperatures (around 100 °C). Gupta *et al* [10] proposed that H_2O-solvated Pd^{2+}-2Z sites are the adsorption sites for NO at 100 °C, which are not affected by H_2O. They also state that the NO adsorption on hydrolyzed $Pd(OH)^+$ sites would be inhibited due to the blockage by H_2O [10]. However, the $Pd(OH)^+$ can adsorb the NO with the formation of NO_2 after the desorption of H_2O with the temperature increasing to 100-200 °C range [8, 10]. This can be illustrated in the following equation.

$$2\ Pd(OH)^+ + 3NO = 2\ Pd^+\text{-}NO + NO_2 + H_2O \qquad (1)$$

In this sense, the decrease of the NO adsorption and the NO_2 formation at around 160 °C should be attributed to the decline of the $Pd(OH)^+$ after HTA treatment (Fig. 7). However, there seems a contradiction in our NO adsorption (Fig. 1) and CO-DRIFTs results (Fig. 7), which shows that 1 Pd (6)-750 and 1 Pd (13)-800, where the $Pd(OH)^+$ is dominate and Pd^{2+}-2Z almost disappear (Fig. 7), still exhibit high NO adsorption capacity at 100 °C (Fig. 1). It worth pointing that the CO-DRIFTs measurements in Fig. 7 were conducted in the absence of H_2O, which only presents the end state of Pd in the dehydrated catalysts. While the Pd ions are solvated and mobilized by H_2O molecules during the NO adsorption in the presence of H_2O in Fig. 1 [39]; thus, the location and the state of Pd should be different from that shown in CO-DRIFTs in Fig. 7. The NO adsorption (Fig. 1) and CO-DRIFTs (Fig. 7) results indicate that the $Pd(OH)^+$ in dehydrated HTA catalysts might transform to H_2O-solvated Pd^{2+}-2Z in the presence of H_2O, resulting in the decrease of the NO_x adsorption peaks at 160 °C (Fig. 1). On the other hand, back to Eq.1, two monomeric $Pd(OH)^+$ sites are needed to complete the NO adsorption and the NO oxidation to NO_2 at 160 °C [8, 10]. Therefore, we speculate that the decrease of the Pd cations density after

HTA (Fig. 10) might affect the participation of two Pd cations in Eq. 1 at the same time. This might also be the reason for eliminating the pathway of NO adsorption and NO_2 formation at 160 °C.

4.2. *Effect of Al Detachment on Deactivation*

As is well known that framework Al provide the ion exchange sites for Pd cations [14, 16, 36]. Therefore, Al detachment resulting in the diminishment of the ion-exchange sites is considered the primary reason for the agglomeration of Pd^{2+} ions to PdO in Pd/SSZ-13, as proposed in previous works [16-18, 21]. Indeed, the ^{27}Al MAS NMR results in our work (Fig. 4) show a decline in TFAl content in both 1 Pd (6) and 1 Pd (13) after HTA treatment. At the same time, the Pd^{2+} ions content is also decreased (Fig. 6). However, the 1 Pd (6) and 1 Pd (13) show a similar dealumination (Fig. 4) but exhibit different degrees of Pd^{2+} ions decline (quantified and normalized using results in Table S3 and S4) after HTA, as shown in Fig. 10a. Furthermore, to illustrate the relationship between dealumination and the decline of ionic Pd after HTA, the Pd^{2+} cations loss as a function of dealumination were plotted in Fig. 10b. It shows that the decline of Pd cations do not vary linearly with the extent of Al detachment in both 1 Pd (6) and 1 Pd (13) samples, indicating that both factors only have a weak correlation. Next, the relationship between dealumination and Pd^{2+} ions agglomeration is analyzed depending on the HTA temperature.

The Pd/Al ratio of 1 Pd (6) and 1 Pd (13) is 0.05 and 0.11, respectively, much lower than the ideal Pd/Al ratio of 0.5, indicating that most of the framework Al is not occupied by Pd cations but stay as Si-O(H)-Al. Recently, Lee *et al.* [41] reported that around 80% of framework Al was detached, but PdO was not formed in a Pd/SSZ-13 after HTA at 750 °C, indicating that the dealumination is due to the loss of Al in Si-O(H)-Al instead of the Pd^{2+} occupied Si-O-Al sites. Also, a similar phenomenon was found by Wang *et al.* [21]. They showed that, in the NH_3-TPD characterization for Pd/SSZ-13, the NH_3 desorption from Pd cations was not changed, but the NH_3 desorption from Brønsted acid sites was diminished significantly after HTA at 800 ºC [21]. It is known that Brønsted acid sites in zeolites are the most vulnerable sites attacked by H_2O during HTA [42, 43]. Therefore, Pd exchanged framework Al sites would show higher stability than Si-O(H)-Al, by removing the hydroxyl prone to hydrolyzed [43]. Similar to Lee *et al.* [41] and Wang *et al.* [21], in our case, a large content of framework Al (around 30%) is detached in 1 Pd (13) after HTA at 800 ºC, while only minor Pd^{2+} content decline (16%) was observed (Fig. 10). Therefore, the dealumination in 1 Pd (13) might be primarily attributed to the Si-O(H)-Al hydrolysis, instead of ionic Pd occupied Al sites, after HTA at 800 ºC, which can be supported by the NH_3-DRIFTs results in Fig. 5. For a more intuitive understanding, the schemes of this process are shown in Fig. 11. The above argument indicates that the decrease of ion-exchange sites due to dealumination, if it is one of the contributions, should not be the primary reason for the agglomeration of Pd^{2+} ions after HTA at 800 ºC. The deactivation of 1 Pd (6)-800 will be discussed in section 4.3.

A similar extent of framework Al (around 40%) is detached in both 1 Pd (6) and 1 Pd (13) samples after HTA at 850 ºC, while Pd^{2+} ions loss degrees are different (76% *v.s.* 32%) (Fig. 10a). This contradiction suggests that Al detachment should also not be the primary reason for Pd^{2+} agglomeration for the samples aged at 850 ºC. The dealumination would undoubtedly result in the serious Pd^{2+} agglomeration to PdO only after HTA at 900 ºC, where most of the Al sites (including the Pd occupied Al and the Brønsted acid sites) are detached (Fig. 4 and Fig, 5). However, some other factors should play an important role in Pd^{2+} agglomeration and the resultant NO storage capacity decline of Pd/SSZ-13 after HTA at 800/850 ºC.

4.3 Effect of Pd Mobility on the Deactivation

The migration of Pd cations is observed during HTA at 800 and 850 °C, as shown in CO-DRIFTs (Fig. 7). It indicates that Pd cations are not fixed by the framework Al sites, instead, the Pd cations are mobile during HTA. The hydrolysis and migration of Pd cation under steam were widely reported in previous studies [17, 18, 44-47]. It is proposed that the Pd ions were first hydrolyzed to $Pd(OH)_2$, likely following Eq. 2 and 3, which weakens the interaction between the cations and the framework, favoring the movement of the cations during HTA [18, 45]. Furthermore, CO-DRIFTs (Fig. 7) results show that peak for $Pd(OH)^+$ at 2161 cm^{-1} increased in 1 Pd (6) and 1 Pd (13) after HTA at 800 and 800/850 ºC, respectively, indicating that a part of the hydrolyzed Pd cation would lose the H_2O and coordinated to the framework again during HTA, following Eq. 4. On the other hand, some mobile $Pd(OH)_2$ intermediates would also be collided to PdO *via* a dihydroxylation-condensation, analogous to the agglomeration process of hydrolysis Cu^{2+} ions to CuO_x [26], following Eq. 5.

$$Pd^{2+}\text{-}2Z + H_2O \rightarrow Pd(OH)_2 + 2\ H^{+}\text{-}Z \qquad (2)$$

$$Pd(OH)^{+}\text{-}Z + H_2O \rightarrow Pd(OH)_2 + H^{+}\text{-}Z \qquad (3)$$

$$Pd(OH)_2 + H^{+}\text{-}Z \rightarrow Pd(OH)^{+}\text{-}Z + H_2O \qquad (4)$$

$$Pd(OH)_2 + Pd(OH)_2 \rightarrow 2\ PdO + 2\ H_2O \qquad (5)$$

$$2\ PdO + 2\ H_2O \rightarrow Pd(OH)_2 + Pd(OH)_2 \qquad (6)$$

$$Pd(OH)_2 + H^{+}\text{-}Z \rightarrow Pd(OH)^{+}\text{-}Z + H_2O \qquad (7)$$

$$Pd(OH)_2 + 2\ H^{+}\text{-}Z \rightarrow Pd^{2+}\text{-}2Z + H_2O \qquad (8)$$

In contrast to our results showing that Pd^{2+} ions are agglomerated to PdO (Fig. 8 and 9), Ryou *et al.* [18] found that HTA at 800 °C would increase the Pd cations content in Pd/SSZ-13 through hydrolyzation of PdO nanoparticles to Pd cations following Eqs. 6-8. This indicates that the transformation of different kinds of Pd following Eqs. 2-8 should be in a transit status. In other words, Pd cations and PdO can be transformed into each other by interacting with the framework during HTA. In this sense, the initial state of Pd in Pd/SSZ-13 would influence the transformation between PdO nanoparticles and Pd cations in Eqs. 1-7. Based on Ryou *et al.* [17, 18], the Pd primarily exist as PdO nanoparticles in the Pd/SSZ-13, while Pd cations are dominant in 1 Pd (6) and 1 Pd (13) in our work (Fig. 6 and 7). Consequently, the Pd cations tend to be agglomerated to PdO after HTA treatment at 800 °C in 1 Pd (6) and 1 Pd (13) samples, while reverse transformation direction of PdO nanoparticles to Pd cations occur in work by Ryou *et al.* [18].

1 Pd (6) sample shows more severe Pd^{2+} ions agglomeration and NO storage decline than 1 Pd (13) after HTA at 800 and 850 °C (Fig. 10). As discussed in section 4.2, the decline of ion-exchange sites by dealumination is not the primary reason for the difference. Instead, the difference between aged 1 Pd (6) and 1 Pd (13) samples should be related to the mutual transformation between PdO and Pd^{2+} ions during HTA, as discussed above. The observed large PdO particles on the external surface of the zeolite (Fig. 8 and 9) suggests that the PdO nanoparticles are also mobile during HTA. It was reported that the Brønsted acid sites stabilize the PdO nanoparticles in Pd/zeolite catalysts [8, 48, 49]. However, on the contrary, in the presence of H_2O, the Brønsted acid sites increase the mobility of palladium nanoparticles, resulting in the sintering of PdO to larger particles [44, 47]. In our case, 1 Pd (6) and 1 Pd (13) show similar extent of dealumination after HTA at 800 and 850 °C (Fig. 10a). However, 1 Pd (6) has a higher Al content than 1 Pd (13). In addition, more Pd^{2+} ions are agglomerated in 1 Pd (6) than 1 Pd (13) after HTA at 800 and 850 °C (Fig. 10a), which should lead to a larger restoration of acid sites in the former samples. These two factors would result in that aged 1 Pd (6) samples have a higher Brønsted acid sites density than aged 1 Pd (13) samples. Therefore, it is expected that the PdO particles in 1 Pd (6) possess a higher mobility than 1 Pd (13) under steam treatment, which are easier sintering to large particles. This speculation can be supported by the TEM

images in Fig. 8 and 9, showing that larger PdO particles are formed in 1 Pd (6) than 1 Pd (13) after HTA at the same temperature. Furthermore, formation of large particles on the external surface of zeolite would eliminate the pathway of PdO redispersed to Pd^{2+} in Pd/SSZ-13 following Eqs. 6-8 [16, 50], resulting in the severe loss of Pd^{2+} ions in 1 Pd (6) after HTA at 800 and 850 °C (Fig. 10).

5. Conclusion

The hydrothermal stability of Pd/SSZ-13 with the same Pd loading (1 wt.%) but different Si/Al ratio (6 *vs.* 13) are compared. The two Pd/SSZ-13 catalysts suffer a similar extent of dealumination after HTA at the same temperature. However, the 1 Pd (6) sample experiences severe structure damage, while the 1 Pd (13) zeolite structure is still well-maintained after HTA, since the larger content of framework Al is detached in the former sample. The agglomeration of Pd^{2+} ions to large PdO particles reduces the NO adsorption sites, decreasing the storage capacity of the HTA samples. The reason for the deactivation of Pd/SSZ-13 varies dependent on the HTA temperature. The severe dealumination would result in deactivation upon aging at 900 ºC. The Pd^{2+} ions agglomeration to PdO after HTA at 800 and 850 ºC cannot be primarily attributed to the decrease of the ion-exchange sites by dealumination, which is more likely related to the mobility of the Pd species.

Acknowledgments

We gratefully acknowledge the scholarship to H.W. Zhao from China Scholarship Council. H.W. Zhao acknowledges the financial support by the National Natural Science Foundation of China (22006044).

Declaration of Competing Interest

The authors declare no competing financial interest.

References

[1] A.M. Beale, F. Gao, I. Lezcano-Gonzalez, C.H.F. Peden, J. Szanyi, Chem. Soc. Rev. 44 (2015) 7371-7405.

[2] Y.J. Kim, J.K. Lee, K.M. Min, S.B. Hong, I.-S. Nam, B.K. Cho, J. Catal. 311 (2014) 447-457.

[3] J. Wang, H. Zhao, G. Haller, Y. Li, Appl. Catal. B: Environ. 202 (2017) 346-354.

[4] H.-Y. Chen, J.E. Collier, D. Liu, L. Mantarosie, D. Durán-Martín, V. Novák, R.R. Rajaram, D. Thompsett, Catal. Lett. 146 (2016) 1706-1711.

[5] Y. Gu, W.S. Epling, Appl. Catal. A: Gen. 570 (2019) 1-14.

[6] Y. Gu, R.P. Zelinsky, Y.-R. Chen, W.S. Epling, Appl. Catal. B: Environ. 258 (2019) 118032.

[7] J. Lee, J.R. Theis, E.A. Kyriakidou, Appl. Catal. B: Environ. 243 (2019) 397-414.

[8] Y. Zheng, L. Kovarik, M.H. Engelhard, Y. Wang, Y. Wang, F. Gao, J. Szanyi, J. Phy. Chem. C 121 (2017) 15793-15803.

[9] K. Khivantsev, F. Gao, L. Kovarik, Y. Wang, J. Szanyi, J. Phy. Chem. C 122 (2018) 10820-10827.

[10] A. Gupta, S.B. Kang, M.P. Harold, Catal. Today (2020) DOI:10.1016/j.cattod.2020.01.018.

[11] K. Khivantsev, N.R. Jaegers, L. Kovarik, J.C. Hanson, F.F. Tao, Y. Tang, X. Zhang, I.Z. Koleva, H.A. Aleksandrov, G.N. Vayssilov, Y. Wang, F. Gao, J. Szanyi, Angew. Chem. Int. Ed. Engl. 57 (2018) 16672-16677.

[12] M. Ambast, K. Karinshak, B.M.M. Rahman, L.C. Grabow, M.P. Harold, Appl. Catal. B: Environ. 269 (2020) 118802.

[13] A. Vu, J. Luo, J. Li, W.S. Epling, Catal. Lett. 147 (2017) 745-750.

[14] K. Khivantsev, N.R. Jaegers, L. Kovarik, S. Prodinger, M.A. Derewinski, Y. Wang, F. Gao, J. Szanyi, Appl. Catal. A: Gen. 569 (2019) 141-148.

[15] J.R. Theis, J.A. Ura, Catal. Today (2020) DOI: 10.1016/j.cattod.2020.01.040.

[16] K. Khivantsev, N.R. Jaegers, L. Kovarik, J.Z. Hu, F. Gao, Y. Wang, J. Szanyi, Emiss. Control Sci. and Technol. (2019).

[17] Y. Ryou, J. Lee, S.J. Cho, H. Lee, C.H. Kim, D.H. Kim, Appl. Catal. B: Environ. 212 (2017) 140-149.

[18] Y. Ryou, J. Lee, H. Lee, C.H. Kim, D.H. Kim, Catal. Today 320 (2019) 175-180.

[19] A. Wang, K. Xie, A. Kumar, K. Kamasamudram, L. Olsson, Catal. Today (2020) DOI: 10.1016/j.cattod.2020.01.035.

[20] Y. Shan, Y. Sun, Y. Li, X. Shi, W. Shan, Y. Yu, H. He, Top. Catal. 63 (2020) 944-953.

[21] A. Wang, K. Lindgren, M. Di, D. Bernin, P.-A. Carlsson, M. Thuvander, L. Olsson, Appl. Catal. B: Environ. 278 (2020) 119315.

[22] Y. Shan, W. Shan, X. Shi, J. Du, Y. Yu, H. He, Appl. Catal. B: Environ. 264 (2020) 118511.

[23] K. Xie, J. Woo, D. Bernin, A. Kumar, K. Kamasamudram, L. Olsson, Appl. Catal. B: Environ. 241 (2019) 205-216.

[24] J.H. Kwak, D. Tran, S.D. Burton, J. Szanyi, J.H. Lee, C.H.F. Peden, J. Catal. 287 (2012) 203-209.

[25] Y. Ma, H. Zhao, C. Zhang, Y. Zhao, H. Chen, Y. Li, Catal. Today (2019) DOI: 10.1016/j.cattod.2019.03.057.
[26] J. Song, Y. Wang, E.D. Walter, N.M. Washton, D. Mei, L. Kovarik, M.H. Engelhard, S. Prodinger, Y. Wang, C.H.F. Peden, F. Gao, ACS Catal. 7 (2017) 8214-8227.
[27] F. Gao, J. Szanyi, Appl. Catal. A: Gen. 560 (2018) 185-194.
[28] H. Zhao, Y. Zhao, Y. Ma, X. Yong, M. Wei, H. Chen, C. Zhang, Y. Li, J. Catal. 377 (2019) 218-223.
[29] X. Chen, J.W. Schwank, G.B. Fisher, Y. Cheng, M. Jagner, R.W. McCabe, M.B. Katz, G.W. Graham, X. Pan, Appl. Catal. A: Gen. 475 (2014) 420-426.
[30] J. Lee, Y. Ryou, S.J. Cho, H. Lee, C.H. Kim, D.H. Kim, Appl. Catal. B: Environ. 226 (2018) 71-82.
[31] H. Zhao, Y. Zhao, M. Liu, X. Li, Y. Ma, X. Yong, H. Chen, Y. Li, Appl. Catal. B: Environ. 252 (2019) 230-239.
[32] J.H. Kwak, R.G. Tonkyn, D.H. Kim, J. Szanyi, C.H.F. Peden, J. Catal. 275 (2010) 187-190.
[33] Y. Shan, J. Du, Y. Yu, W. Shan, X. Shi, H. He, Appl. Catal. B: Environ. 266 (2020) 118655.
[34] S. Prodinger, M.A. Derewinski, Y. Wang, N.M. Washton, E.D. Walter, J. Szanyi, F. Gao, Y. Wang, C.H.F. Peden, Appl. Catal. B: Environ. 201 (2017) 461-469.
[35] A. Wang, P. Arora, D. Bernin, A. Kumar, K. Kamasamudram, L. Olsson, Appl. Catal. B: Environ. 246 (2019) 242-253.
[36] K. Khivantsev, N.R. Jaegers, I.Z. Koleva, H.A. Aleksandrov, L. Kovarik, M. Engelhard, F. Gao, Y. Wang, G.N. Vayssilov, J. Szanyi, J. Phy. Chem. C 124 (2019) 309-321.
[37] K. Khivantsev, X.Y. Wei, L. Kovarik, N.R. Jaegers, E.D. Walter, P. Tran, Y. Wang, J. Szanyi, ChemRxiv. Preprint. https://doi.org/10.26434/chemrxiv.12385577.v1.
[38] K. Khivantsev, N.R. Jaegers, I.Z. Koleva, H.A. Aleksandrov, L. Kovarik, M. Engelhard, F. Gao, W. Yong, G.N. Vayssilov, J. Szanyi, ChemRxiv. Preprint. https://doi.org/10.26434/chemrxiv.7789454.v2.
[39] K. Mandal, Y. Gu, K.S. Westendorff, S. Li, J.A. Pihl, L.C. Grabow, W.S. Epling, C. Paolucci, ACS Catal. (2020) 12801-12818.
[40] H. Zhao, X. Chen, A. Bhat, Y. Li, J.W. Schwank, Appl. Catal. B: Environ. 282 (2021) 119611.
[41] J. Lee, J. Kim, Y. Kim, S. Hwang, H. Lee, C.H. Kim, D.H. Kim, Appl. Catal. B: Environ. 277 (2020) 119190.
[42] S. Malola, S. Svelle, F.L. Bleken, O. Swang, Angew. Chem. Int. Ed. Engl. 51 (2012) 652-655.
[43] F. Gao, Y. Wang, N.M. Washton, M. Kollár, J. Szanyi, C.H.F. Peden, ACS Catal. 5 (2015) 6780-6791.
[44] I. Friberg, N. Sadokhina, L. Olsson, Appl. Catal. B: Environ. 250 (2019) 117-131.
[45] H. Ohtsuka, T. Tabata, Appl. Catal. B: Environ. 21 (1999) 133-139.
[46] J. Lee, Y. Ryou, S. Hwang, Y. Kim, S.J. Cho, H. Lee, C.H. Kim, D.H. Kim, Catal. Sci. Technol. 9 (2019) 163-173.
[47] A.W. Petrov, D. Ferri, F. Krumeich, M. Nachtegaal, J.A. van Bokhoven, O. Krocher, Nature Commun. 9 (2018) 2545.
[48] A.W. Aylor, J.A. Reimer, A.T. Bell, J. Catal. 172 (1997) 453-462.

[49] K. Okumura, J. Amano, N. Yasunobu, M. Niwa, J. Phys. Chem. B 104 (2000) 1050-1057.
[50] Y. Ryou, J. Lee, Y. Kim, S. Hwang, H. Lee, C.H. Kim, D.H. Kim, Appl. Catal. A: Gen. 569 (2019) 28-34.

Table 1. Pd loading content and NO storage capacity (NO/Pd) for fresh and aged Pd/SSZ-13 samples.

Samples	1 Pd (6)	1 Pd (6)-800	1 Pd (6)-850	1 Pd (6)-900	1 Pd (13)	1 Pd (13)-800	1 Pd (13)-850	1 Pd (13)-900
Pd content [a] (wt.%)	1.02	-	-	-	0.99	-	-	-
NO/Pd [b] ratio	0.70	0.42	0.18	0.05	0.59	0.48	0.40	0.17

a. Determined by ICP-OES.

b. Acquired from Fig. 1.

Table 2. S_{BET}, S_{micro}, S_{pore}, S_{meso}, and V_{micro} for fresh and aged Pd/SSZ-13 samples.

Samples	1 Pd (6)	1 Pd (6)-800	1 Pd (6)-850	1 Pd (6)-900	1 Pd (13)	1 Pd (13)-800	1 Pd (13)-850	1 Pd (13)-900
S_{BET} [a] (m^2/g)	457	283	281	124	462	486	549	523
S_{micro} [b] (m^2/g)	417	248	238	113	444	462	507	463
V_{pore} [b] (cm^3/g)	0.25	0.17	0.16	0.07	0.28	0.29	0.32	0.31
V_{meso} [b] (cm^3/g)	0.02	0.04	0.04	0.01	0.06	0.06	0.07	0.08
V_{micro} [b] (cm^3/g)	0.23	0.13	0.12	0.06	0.22	0.23	0.25	0.23

a. Surface area was calculated using the BET equation

b. Estimated using the t-plot method.

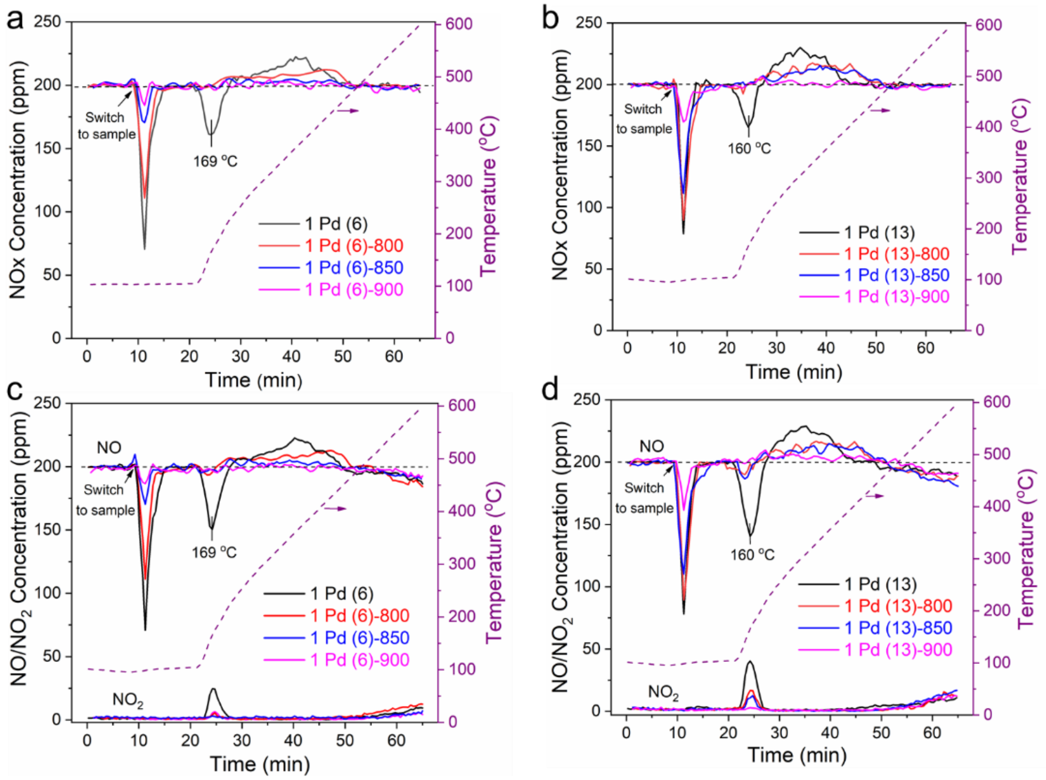

Fig. 1. The NO_x profiles of 1 Pd (6) (a) and 1 Pd (13) (b) for NO adsorption at 100 °C for 10 min followed with release (10 °C/min up to 600 °C). The concentrations of NO and NO_2 of 1 Pd (6) (c) and 1 Pd (13) (d) during adsorption and release.

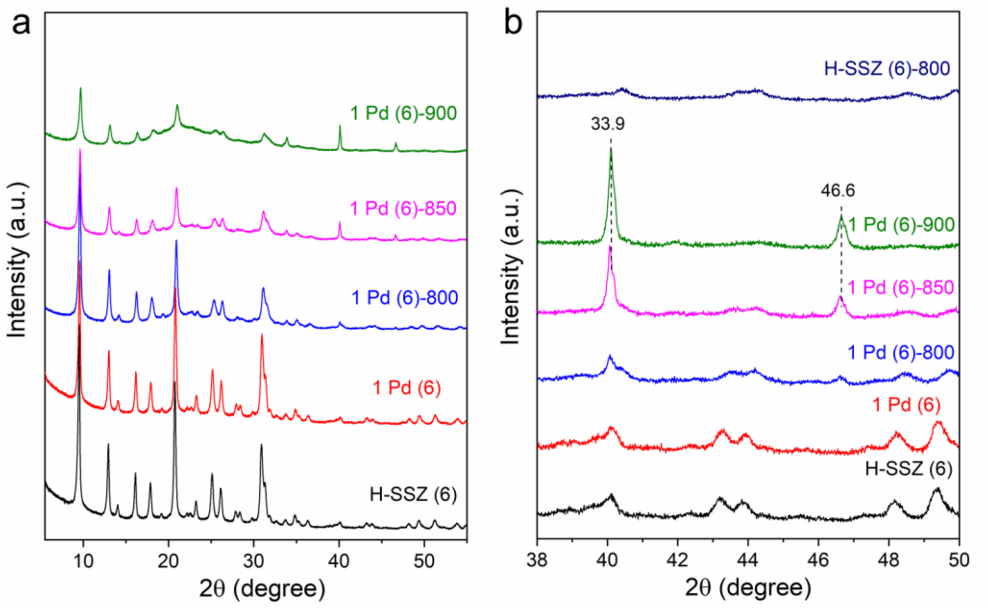

Fig. 2. (a) XRD patterns of fresh and HTA 1 Pd (6) samples. (b) Enlarged XRD patterns in 38-50º.

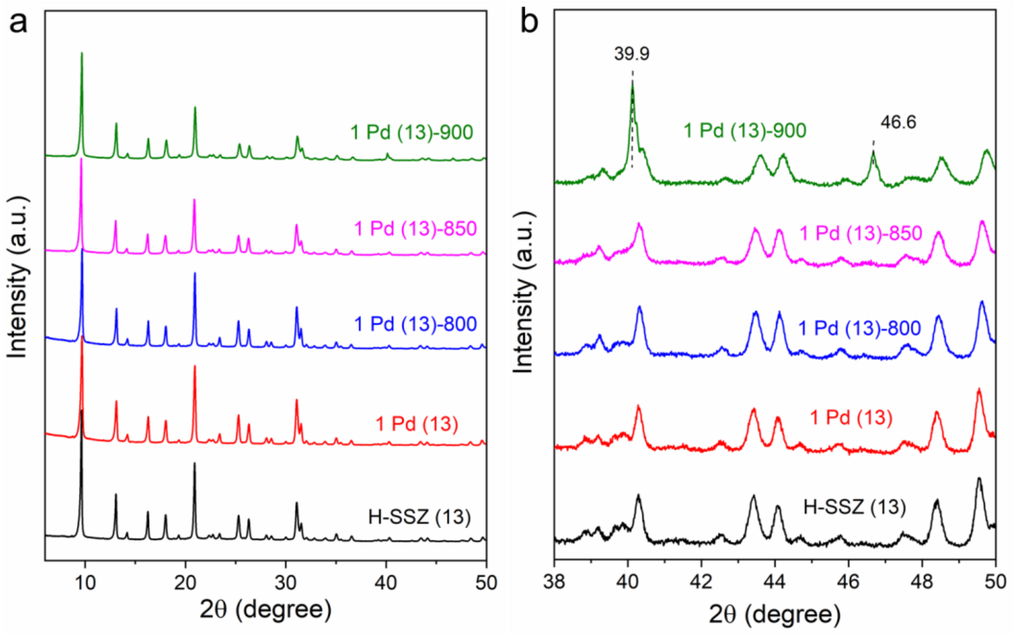

Fig. 3. (a) XRD patterns of fresh and HTA 1 Pd (13) samples. (b) Enlarged XRD patterns in 38-50º.

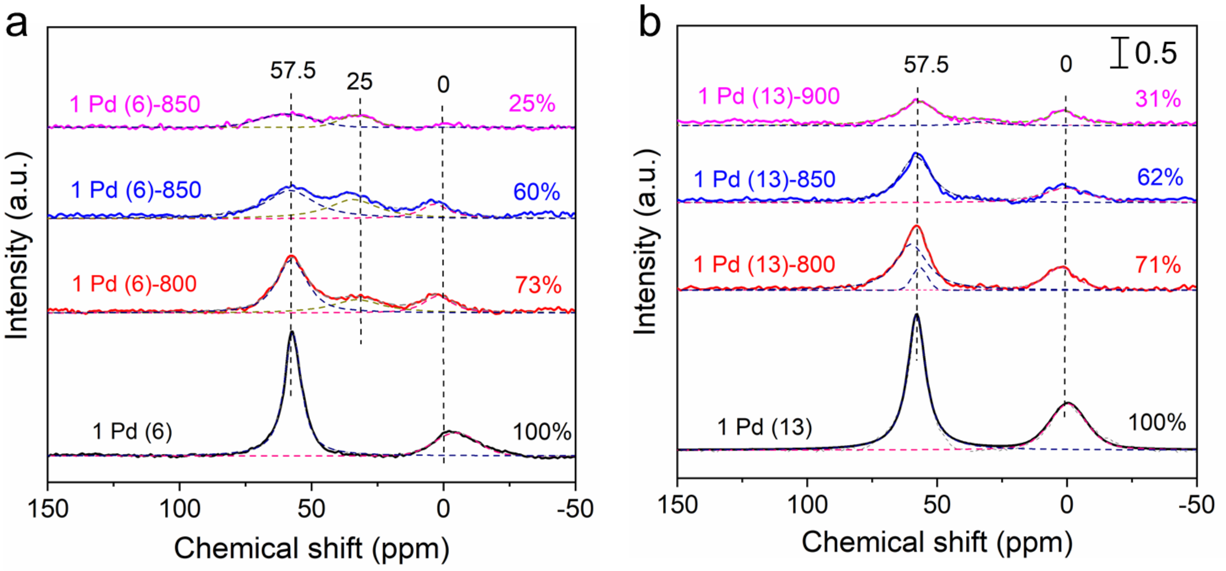

Fig. 4. Solid state ^{27}Al MAS NMR spectra of the (a) fresh and HTA 1 Pd (6) catalysts; (b) fresh and HTA 1 Pd (13) catalysts. The deconvolution method of the ^{27}Al MAS NMR is Lorentzian/Gaussian.

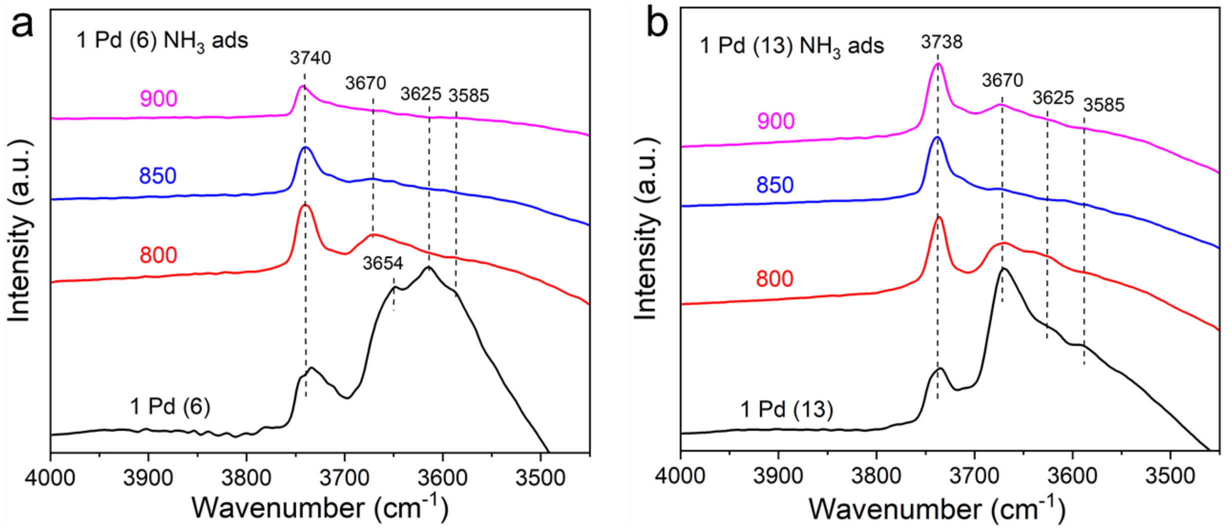

Fig. 5. (a) NH_3-DRIFTs spectra of fresh and HTA 1 Pd (6) samples. (b) NH_3-DRIFTs spectra of fresh and HTA 1 Pd (13) catalysts. The spectra were collected in N_2 at 25 ºC.

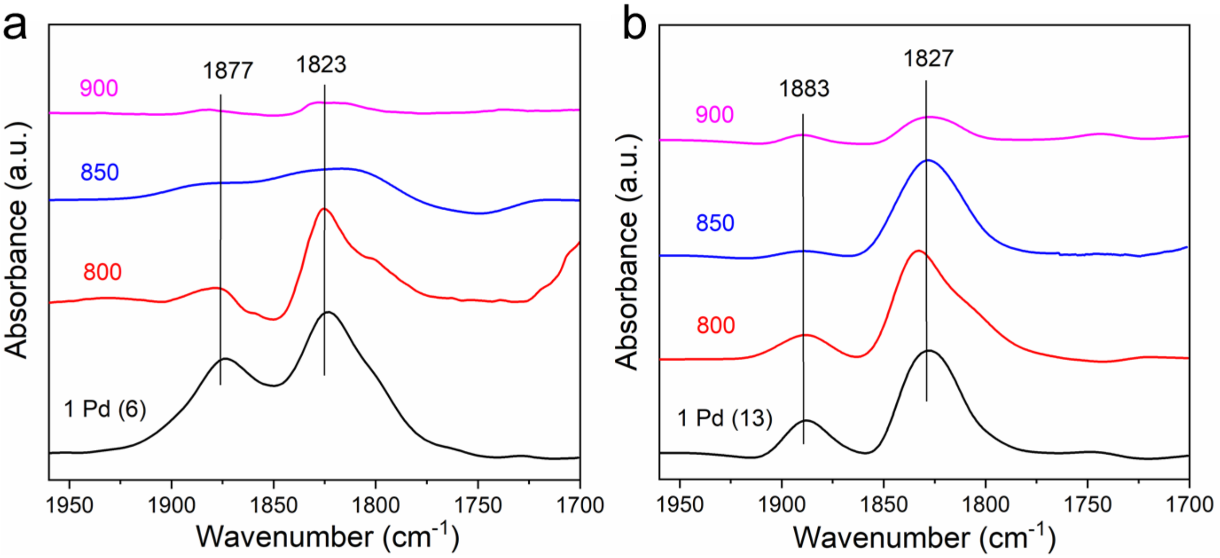

Fig. 6. (a) NO-DRIFTs spectra of fresh and HTA 1 Pd (6) samples. (b) NO-DRIFTs spectra of fresh and HTA 1 Pd (13) catalysts. The spectra were collected in 20%O_2/N_2 at 25 ºC.

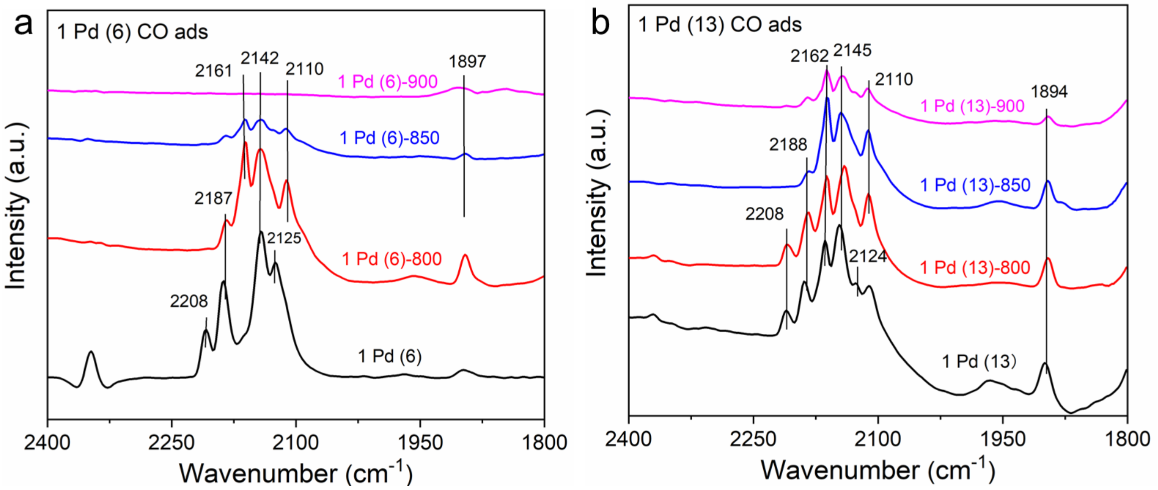

Fig. 7. (a) CO-DRIFTs spectra of fresh and HTA 1 Pd (6) samples. (b) CO-DRIFTs spectra of fresh and HTA 1 Pd (13) catalysts. The spectra were collected in N_2 at 25 ºC.

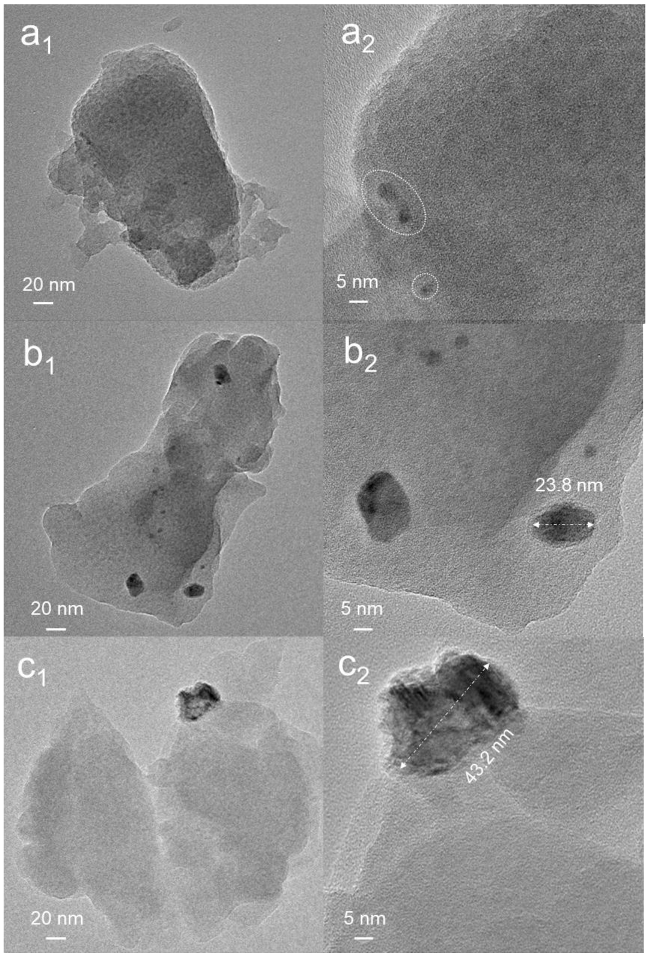

Fig. 8. TEM images of (a) 1 Pd (6)-800, (b) 1 Pd (6)-850, and (c) 1 Pd (6)-900.

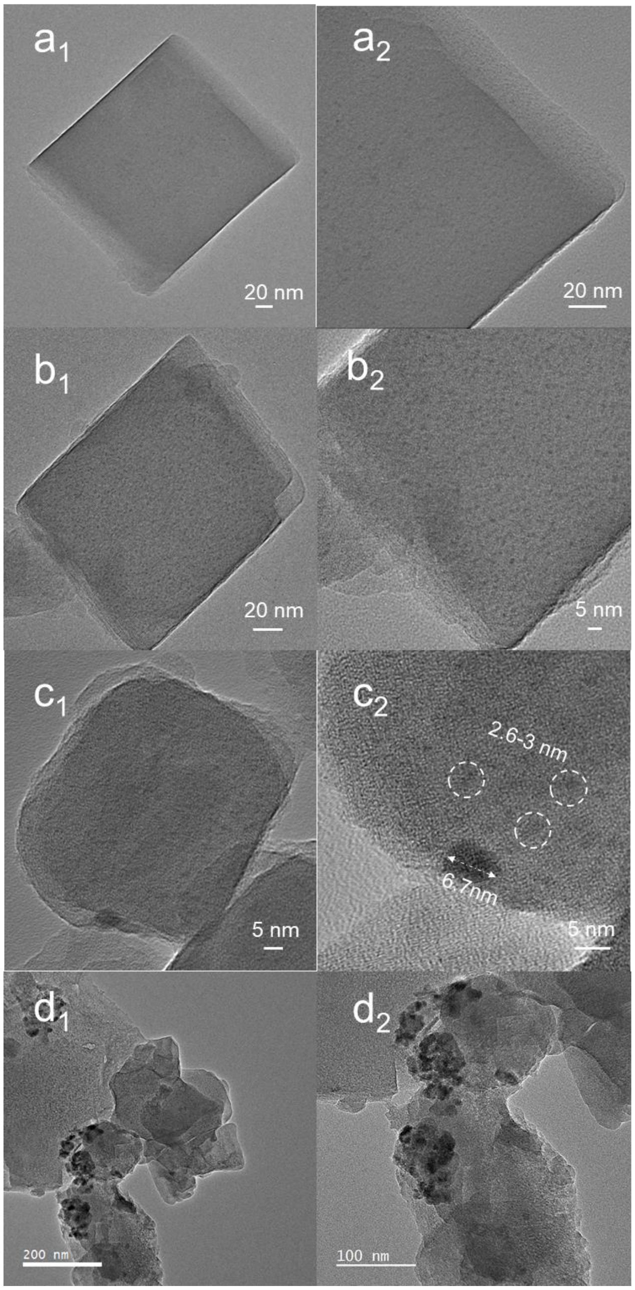

Fig. 9. TEM images of (a) 1 Pd (13), (b) 1 Pd (13)-800, (c) 1 Pd (13)-850, and (d) 1 Pd (13)-900.

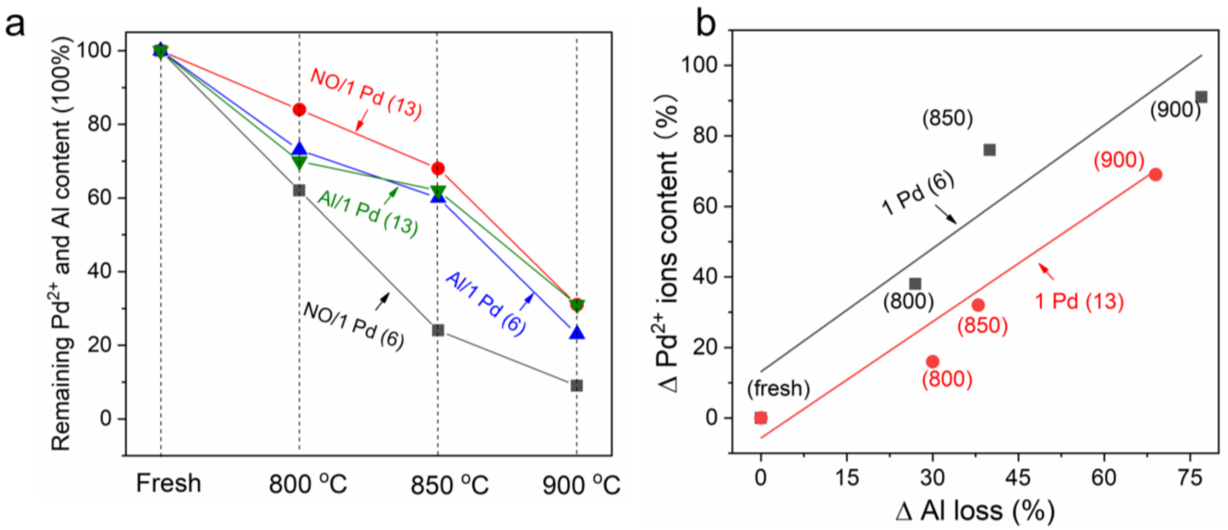

Fig. 10. (a) The normalized content of TFAl and Pd cations in 1 Pd (6) and 1 Pd (13) after aging at different temperatures. (b) The decline of Pd^{2+} ions as a function of TFAl loss after HTA. The Pd^{2+} ions content in fresh and HTA 1 Pd (6) and 1 Pd (13) samples is normalized using results in Table S3 and S4, with the fresh samples as reference. The normalized TFAl content in each sample is obtained in Fig. 4.

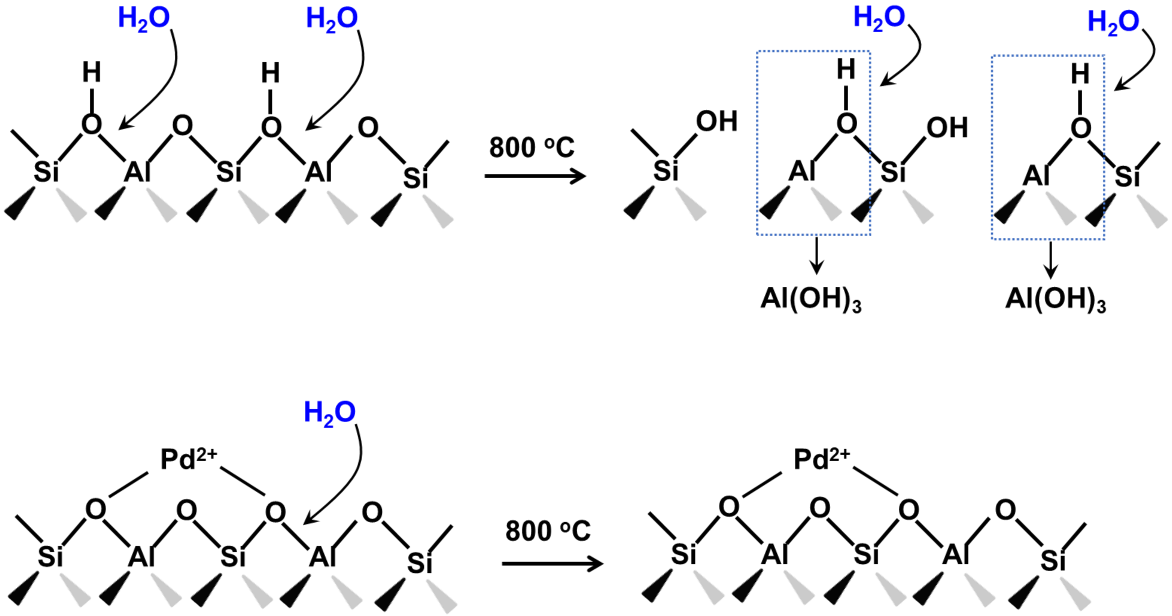

Fig. 11. Schemes of hydrolysis process of Si-OH-Al sites and Pd occupied Al sites during HTA.

Graphical Abstract

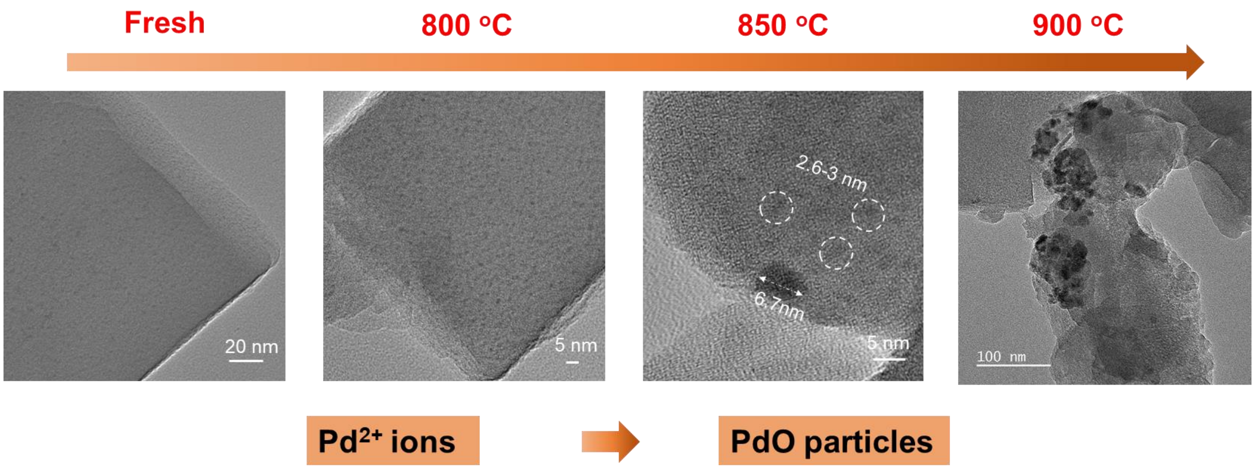

Highlights

- Pd/SSZ-13 suffers deactivation due to Pd^{2+} agglomeration to PdO after aging.
- Pd tend to move toward outside of zeolite and to agglomerate to large PdO particles.
- Dealumination results in Pd^{2+} ions agglomeration after aging at 900 ºC.
- The Pd mobility results in deactivation after aging at 800/850 ºC.